NANO LETTERS

Communication

HELICITY SENSITIVE PLASMONIC TERAHERTZ INTERFEROMETER

Yakov Matyushkin, Sergey Danilov, Maxim Moskotin, Vsevolod Belosevich, Natalia Kaurova, Maxim Rybin, Elena D. Obraztsova, Georgy Fedorov, Ilya Gorbenko, Valentin Kachorovskii, and Sergey D. Ganichev

Nano Lett., **Just Accepted Manuscript** • DOI: 10.1021/acs.nanolett.0c02692 • Publication Date (Web): 09 Sep 2020

is published by the American Chemical Society. 1155 Sixteenth Street N.W., Washington, DC 20036

HELICITY SENSITIVE PLASMONIC TERAHERTZ INTERFEROMETER

Yakov Matyushkin,[†,‡,¶,§] Sergey Danilov,[‡] Maxim Moskotin,[†,¶] Vsevolod Belosevich,[†,¶] Natalia Kaurova,[¶] Maxim Rybin,[†,‖] Elena D. Obraztsova,[†,‖] Georgy Fedorov,[*,†,¶] Ilya Gorbenko,[⊥,#] Valentin Kachorovskii,[⊥,@] and Sergey Ganichev[*,‡,@]

†*Moscow Institute of Physics and Technology National Research University, 141700 Dolgoprudny, Russia*
‡*Terahertz Center, University of Regensburg, D-380106 Regensburg, Germany*
¶*Physics Department, Moscow State Pedagogical University, 119435 Moscow, Russia*
§*National Research University Higher School of Economics, 101000 Moscow, Russia*
‖*Prokhorov General Physics Institute, RAS, 119991, Moscow, Russia*
⊥*Ioffe Institute, 194021 St. Petersburg, Russia*
#*ITMO University, 197101 St. Petersburg, Russia*
@*CENTERA Laboratories, Institute of High Pressure Physics, PAS, 01-142 Warsaw, Poland*

E-mail: fedorov.ge@mipt.ru; sergey.ganichev@physik.uni-regensburg.de

Abstract

Plasmonic interferometry is a rapidly growing area of research with a huge potential for applications in the terahertz frequency range. In this Letter, we explore a plasmonic interferometer based on graphene Field Effect Transistor connected to specially designed antennas. As a key result, we observe helicity- and phase-sensitive conversion of circularly-polarized radiation into dc photovoltage caused by the plasmon-interference mechanism: two plasma waves, excited at the source and drain part of the transistor interfere inside the channel. The helicity sensitive phase shift between these waves is achieved by using an asymmetric antenna configuration. The dc signal changes sign with inversion of the helicity. A suggested plasmonic interferometer is capable of measuring the phase difference between two arbitrary phase-shifted optical signals. The observed effect opens a wide avenue for phase-sensitive probing of plasma wave excitations in two-dimensional materials.

Keywords

plasmonic interferometer, terahertz radiation, radiation helicity, graphene

Introduction

Interference is in heart of quantum physics and classical optics, where wave superposition plays a key role.[1–3] Besides fundamental significance, interference has very important applied aspects. Optical and electronic interferometers are actively used in modern electronics, and the range of applications is extremely wide and continuously expanding. In addition to standard applications in optics and electronics,[1–3] exciting examples include multiphoton entanglement,[4] nonperturbative multiphonon interference,[5,6] atomic and molecular interferometry[7–9] with recent results in cold-atoms-based precision interferometry,[10] neutron interferometry,[11] interferometers for medical purposes,[12] interference analysis of turbulent states,[13] qubit interferometry[14] with a recent analysis of the Majorana qubits,[15] numerous amazing applications in the astronomy,[16–19] such as interferometers for measuring of gravitational waves[17,18] and antimatter wave interferometry,[19] etc.

Recently, a new direction, plasmonic interferometry,[20–32] has started to actively develop. The plasma wave velocity in 2D materials is normally an order of magnitude larger than the electron drift velocity and is much smaller than the speed of light. Hence, the plasmonic submicron-sized interferometers based on 2D materials are expected to operate efficiently in the terahertz (THz) frequency range.[33,34] In particular, it has been predicted theoretically that a field-effect transistor (FET) can serve as a simple device for studying plasmonic interference effects.[35–38] Specifically, it was suggested that a FET with two antennas attached to the drain and source shows a dc current response to circularly polarized THz radiation which is partially driven by the interference of plasma waves and by helicity of incoming radiation. The first experimental hint on the existence of such an interference contribution was reported in Ref. [35] for an industrial FET, where helicity-driven effects were obtained due to unintentional peculiarities of contact pads. Despite the first successes, creation of effective plasmonic interferometers is still a challenging task although in many aspects plasmonic-related THz phenomena are sufficiently well studied[39–52] with some commercial applications already in the market. The appearance of graphene opened rout for a novel class of active plasmonic structures[53] promising for plasmonic interferometry due to non-parabolic dispersion of charge carriers and support of weakly decaying plasmonic excitations.[54] Plasmonic effects in graphene were already used for the creation of on-chip terahertz spectrometer.[55] Furthermore, the long-standing problem of current-induced THz emission actively discussed starting from Ref. [39] is more likely to be solved by using graphene structures (see discussion in Ref. [56]).

In this Letter, we explore an all-electric tunable — by the gate voltage — plasmonic interferometer based on graphene FET connected to specially designed antennas. Our interferometer demonstrates the helicity-driven conversion of incoming circularly-polarized radiation into phase- and helicity-sensitive dc photovoltage signal. The effect is detected at room- and liquid helium-temperatures for radiation frequencies 0.69 and 2.54 THz. All our results show the plasmonic nature of the effect. Specifically, the rectification of the interfering plasma waves leads to dc response, which is controlled by the gate voltage and encodes information about helicity of the radiation and phase difference between the plasmonic signals. A remarkable feature of this plasmonic interferometer is that there is no need to create an optical delay line, which has to be comparable with the quite large wavelength of the THz signal. By contrast, in this setup, the phase shift between the plasma waves excited at the source and drain electrodes of the FET is maintained by a combination of the antenna geometry and the radiation helicity. It remains finite even in the limit of infinite wavelength and changes sign with inversion of the radiation helicity. The plasmonic interferometer concept realized in our work opens a wide avenue for phase-sensitive probing of plasma wave excitations in two-dimensional materials.

Devices and measurements

The single-layer graphene (SLG), acting as the conducting channel of a FET, was synthesized in a home-made cold-wall chemical vapor deposition reactor by chemical vapor deposition (CVD) on a copper foil with a thickness of 25 μm.[57] SLG was transferred onto an oxidized silicon wafer.[58] The antenna sleeves were attached to the source and drain electrodes. To realize the helicity sensitive terahertz plasmonic interferometer, the antenna sleeves were bent by 45° as shown in Fig. 1b. The sleeves were made using photolithographic methods and metallization sputtering (Ti/Au,

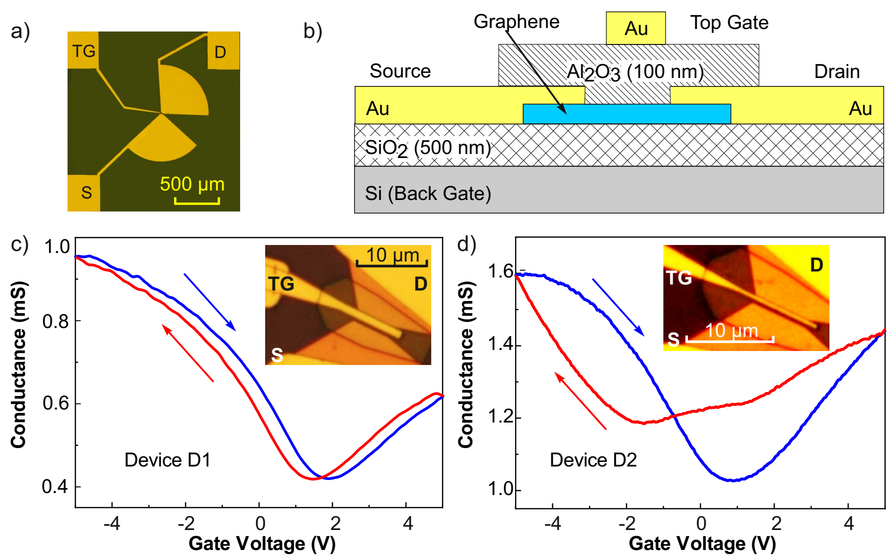

Figure 1: Devices configuration and characterization. (a) Optical image illustrating the device layout with source and drain electrodes connected to sleeves of a bent bow-tie antenna. (b) Structures cross-section showing relative location of the source, drain and top gate electrodes as well as thickness of the dielectric layers. (c,d) Transfer characteristics of devices 1 and 2, respectively. For different directions of the gate voltage sweep as well as the sample cooldowns, the charge neutrality point (CNP) can occur at different gate voltages U_g. Therefore, throughout the paper we indicate range of U_g corresponding to the CNP instead of providing its exact value. Using the Drude formula, we estimate scattering times of the order of 10-20 fs for, e.g., device 1 at room temperature. The curves are measured at a bias voltage of 10 mV. The data are presented for two directions of the gate voltage sweeps, which yield different positions of the CNP. Insets show zoomed images of the devices.

5/100 nm). The resulting structure is sketched in the Figure 1a. Two devices with channel lengths 2 μm (device 1) and 1 μm (device 2) were fabricated with transport characteristics shown in the Figs. 1c and 1d (see Suppl. Material). Zoomed images of the channel parts are shown in insets in Figs. 1c and 1d. Note that for both devices the gates are deposited asymmetrically in respect to the channel. They cover about 75% (device 1) and 50% (device 2) of the channels and the gate stripes are located closer to the drain contact pads.

The experiments have been performed applying a continuous wave methanol laser operating at frequencies $f_1 = 2.54$ THz (wavelength $\lambda_1 = 118$ μm) with a power of $P \approx 20$ mW and $f_2 = 0.69$ THz (wavelength $\lambda_2 = 432$ μm) with $P \approx 2$ mW.[59,60] The laser spot with a diameter of about 1-3 mm is substantially larger than the sample size ensuring uniform illumination of both antennas. The radiation polarization state was controlled by lambda-half plate that rotated the polarization direction of linear polarized radiation and by lambda-quarter plate that transformed linearly polarized radiation into elliptically polarized one.

The helicity of the radiation is then controlled via changing the angle ϕ between the laser polarization and the main axes of the lambda-quarter plate, so that for $\phi = 45°$ the radiation is right circularly polarized (σ^+) and for $\phi = 135°$ — left circularly polarized (σ^-). The functional behavior of the Stokes parameters upon rotation of the waveplates is summarized in the Suppl. Material, see also Ref. [61].

Results

The principal observation made in our experiment is that for all investigated devices the response to circularly polarized radiation crucially depends on its helicity. Fig. 2 displays the response voltage U normalized by the radiation intensity as a function of the angle ϕ obtained under different conditions. We emphasize the significant difference in the signal for $\phi = 45°$ and 135°, corresponding to opposite helicities of circularly polarized light, in particular, the sign inversion observed under some conditions, see e.g. Fig. 2d. The effect is observed for radiation with frequencies 2.54 and 0.69 THz in a wide temperature range from 4.2 K to 300 K. The overall dependence of the signal on an angle ϕ is more complex and is well described by

$$\begin{aligned} U(\phi) &= U_{\rm C}\sin(2\phi) + U_{\rm L1}\sin(4\phi)/2 \\ &+ U_{\rm L2}[\cos(4\phi)+1]/2 + U_0, \end{aligned} \quad (1)$$

where $U_{\rm C}$, $U_{\rm L1}$, $U_{\rm L2}$, and U_0 are fit parameters depending on gate voltage, temperature, and radiation frequency. Note that trigonometric functions used for the fit are the radiation Stokes parameters describing the degree of the circular and linear polarization (see Suppl. Material).[61–63] While three last terms are insensitive to the radiation helicity the first term is π-periodic and describes helicity-sensitive response: it reverses the sign upon switching from right- (σ^+) to left- (σ^-) handed circular polarization. Figure 2 reveals that this term gives a substantial contribution to the total signal. As we show below the π-periodic term is related to the plasma interference in the graphene-based FET channel. Measurements at room and low T demonstrate that cooling the device increases the amplitude of the circular photoresponse by more than ten times, see Figs. 2a and 2b as well as 2d and 2e. The signal increase is also observed by the reduction of radiation frequency, see Figs. 2b and 2c as well as 2e and 2f.

Having experimentally proved the applicability of Eq. (1) and substantial contribution of the helicity driven signal we now concentrate on the dependence of the parameter $U_{\rm C}$ on the gate voltage that controls the type and concentration of the charge carriers in the FET channel. We use the following procedure: we obtain the gate voltage dependence of the response voltage normalized to the radiation power P for two positions of the $\lambda/4$ plate $\phi = 45°$ and 135°, corresponding to opposite helicities of circularly polarized light (σ^+ and σ^-). The half-difference between these two curves directly gives gate voltage dependence of the helicity sensitive photoresponse $U_{\rm C} = (U_{\sigma^+} - U_{\sigma^-})/2$. [see Eq. (1)] The results of these measurements, shown in Fig. 3, reveal that $U_{\rm C}$ is more pronounced at

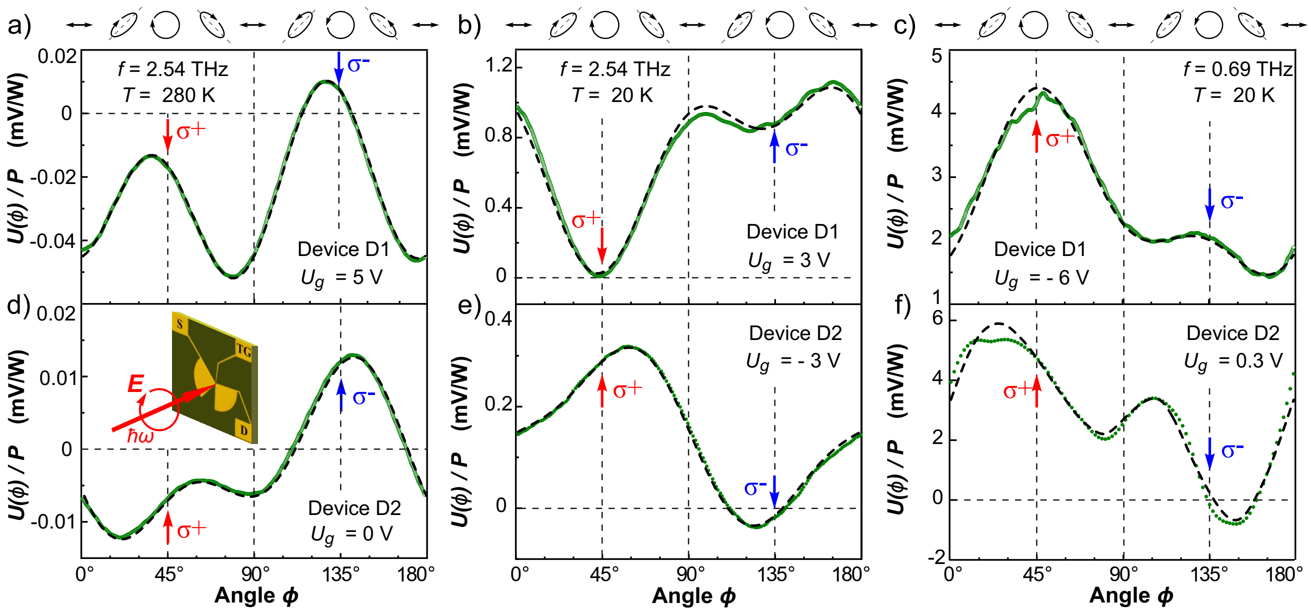

Figure 2: Helicity dependence of the photovoltage $U(\phi)$ normalized by the radiation power P. Photoresponse was measured as the voltage drop U directly over the sample applying lock-in technique at a modulation frequency of 75 Hz. Upper panels (a–c) show the results obtained in device 1 and lower panels (d–f) those in device 2. The data are shown for two radiation frequencies ($f = 2.54$ and 0.69 THz), two temperatures (room temperature and $T = 20$ K) and different gate voltages U_g. Dashed lines show fits according to Eq. (1). The values of the fitting parameters $U_\mathrm{C}, U_\mathrm{L1}, U_\mathrm{L2}$, and U_0 are given in the Suppl. Material. Note that there are two fundamentally different contributions to the response, which are caused by different physical reasons. Regarding the Eqs. (1) and (4), only one term is helicity-sensitive and π-periodic. The helicity-sensitive contribution arises only if the device has the phase asymmetry (even in the absence of asymmetry of amplitudes) while the helicity-insensitive response is caused by asymmetry of the signal amplitudes. These contributions have fundamentally different dependences on light frequency, temperature, and gate voltage. The phase-sensitive contribution dominates in the response when the amplitudes of the waves incident on the drain and source are approximately the same, see Ref. [38]. The ellipses on top illustrate the polarization states at different angles ϕ. The inset sketches the experimental geometry.

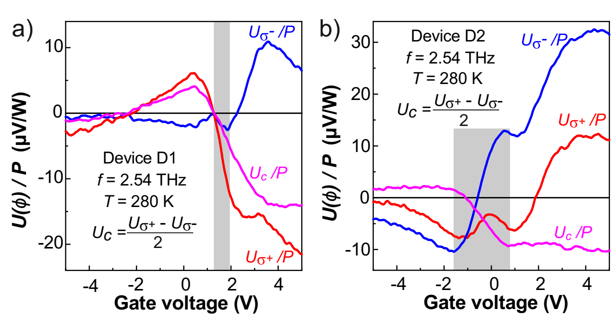

Figure 3: Gate voltage dependencies of the photoresponse of the devices 1 (panel a) and 2 (panel b). Red and blue curves show responses to right- (U_{σ^+}) and left- (U_{σ^-}) handed circularly polarized radiation, respectively. Magenta curve shows the amplitude of the helicity driven response $U_\mathrm{C} = (U_{\sigma^+} - U_{\sigma^-})/2$. Shadowed areas show the range of CNP obtained by transport measurements with different sweeps of the gate voltage U_g, see Figs. 1c and d.

positive gate voltage, where the channel is electrostatically doped with electrons, and changes the sign close to the CNP. The variation of the CNP from measurement to measurement does not allow us to allocate the exact position of the CNP for the gate voltage sweeps during the photoresponse measurements. Note that for device 1, having the gate length twice larger as that of device 2, at large negative gate voltages the second sign inversion of the photocurrent is present. Figure 3a indicates that in device 1 for the whole range of gate voltages photoresponse for σ^+- and σ^-- radiation has consistently opposite sign indicating a negligible contribution of the polarization-independent background. In device 2, however, the background is of the same order as the helicity sensitive response U_C, see Fig. 3b.

Finally, we present additional data on the contributions proportional to fit parameters U_{L1}, U_{L2} and U_0 which are not connected to the radiation helicity and describe the degrees of linear polarization (terms $\propto U_{L1}$ and $\propto U_{L2}$) and radiation intensity (term $\propto U_0$). In experiments applying linearly polarized radiation with a rotation of $\lambda/2$ plate by angle α, the polarization dependence, Eq. (1), takes a form:

$$U(\alpha) = U_{L1}\sin(2\alpha) + U_{L2}\cos(2\alpha) + U_0. \quad (2)$$

An example of the photoresponse variation upon change of α is shown in Fig. 4a. The data reflects the specific antenna pattern of our devices with tilted sleeves. Figure 4b shows the gate voltage dependence of the photoresponse obtained in device 1 for $\alpha = 0$. Comparing these plots with the results for circular photoresponse shows that they behave similarly: in both cases signal changes the sign close to CNP and the response for positive gate voltage, U_g , is larger than that for a negative U_g. Transport measurements carried out parallel to photoresponse measurements show that the photosignal behaves similarly to the normalized first derivative of the conductance G over U_g: $(dG/dU_g)/G$, see Fig. 4a. Note that this behavior is well known for non-coherent, phase-insensitive plasmonic detectors.[50]

Theory and discussion

Conversion of THz radiation into dc voltage can be obtained due to several phenomena including photothermoelectric (PTE) effects,[64–66] rectification on the inhomogeneity of carrier doping in gated structures,[58,66,67] photogalvanic and photon-drag effects[68–70] as well as rectification of electromagnetic waves in a FET channel supporting plasma waves.[40] However, in our experiment only plasmonic mechanism can yield the dc voltage whose polarity changes upon switching the radiation helicity. Indeed, the PTE effects and rectification due to the gradient of carrier doping in gated structures are based on inhomogeneities of either radiation heating or radiation absorption, which are helicity-insensitive. While the circular photocurrents due to the photon drag and photogalvanic effects in the bulk of graphene have been observed previously (see Ref. [70] for review), for present experimental geometry applying normal incident radiation, they are forbidden by symmetry arguments, which allow the circular photocurrents for oblique incidence only.[68–70]

Below, we show that the helicity-sensitive plasmonic response originates from the interference of plasmonic signals excited by the source and drain antenna sleeves. The source and drain potentials with respect to the top gate are given by

$$U_{A,B}(t) = U_{A,B}\cos(\omega t - \varphi_{A,B}), \quad (3)$$

where ω is the radiation frequency. Due to hydrodynamic non-linearity of plasma waves[39,40] DC voltage across the channel appears

$$U = F_1(U_A^2 - U_B^2) + F_2 U_A U_B \cdot \sin(\varphi_A - \varphi_B), \quad (4)$$

where F_1 and F_2 are gate-controlled coefficients which represent, respectively, non-coherent[40] and interference[35–38] contributions to the response [see Eq. (8) below]. They do not depend on signal phases and amplitudes, while all information about coupling with antennas is encoded in factors $(U_A^2 - U_B^2)$ and $U_A U_B \sin(\varphi_A - \varphi_B)$. The amplitudes $U_{A,B}$ and the phase shift between signals, $\varphi_A - \varphi_B$, depend on the radiation polarization and antennas geometry. De-

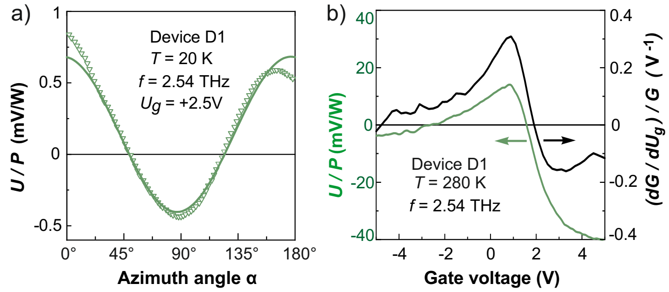

Figure 4: (a) Photovoltage per radiation power as a function of the azimuth angle α. The data are obtained applying linearly polarized radiation with $f = 2.54$ THz for device 1 at $T = 20$ K. Solid line shows fit after Eq. (2) with fitting parameters: $U_{\rm L1}/P = -0.16$, $U_{\rm L2}/P = 0.54$ and $U_0/P = 0.14$ mV/W. (b) Gate voltage dependence obtained for device 1 at $T = 280$ K applying linearly polarized radiation ($\alpha = 0$) with frequency $f = 2.54$ THz (green line). Black line shows gate voltage dependence of the normalized first derivative of the conductance G over $U_{\rm g}$: $(dG/dU_{\rm g})/G$.

sign of our devices, see Fig. 5a, ensures asymmetric coupling of radiation to the source and drain electrodes so that both amplitudes and phases of source and drain potentials are different. When such a bent bow-tie antenna is illuminated by circularly polarized radiation, the source- and drain-related antenna sleeves are polarized with a time delay because of the rotation of the electric field vector.

We use a simplified model, which captures the basic physics of the problem: we replace two antennas shown in Fig. 5a with long thin metallic rods described by vectors $\mathbf{R}_{\rm A,B}$ rotated with respect to the x-axis by geometrical angles of antenna sleeves $\theta_{\rm A,B}$. Assuming that antennas are perfect conductors and neglecting small mutual capacitances, one can write the potentials applied to source and drain as $U_{\rm A,B}(t) = \mathbf{E}(t)\mathbf{R}_{\rm A,B}/2$, where $\mathbf{E}(t) = E_0\,{\rm Re}(\mathbf{e}\,e^{-i\omega t})$ is the time-dependent electric field of impinging wave characterized by amplitude E_0 and polarization vector $\mathbf{e}$. For circularly polarized wave, the phase shift changes sign with changing the helicity of the radiation: $\varphi_{\rm A}-\varphi_{\rm B} = -(\theta_{\rm A}-\theta_{\rm B})$, for $\omega > 0$ (positive helicity) and $\varphi_{\rm A}-\varphi_{\rm B} = \theta_{\rm A}-\theta_{\rm B}$, for $\omega < 0$ (negative helicity). Below, we assume that $\omega > 0$. In order to get equation for $U_{\rm A}^2-U_{\rm B}^2$ and $U_{\rm A}U_{\rm B}\sin(\varphi_{\rm A}-\varphi_{\rm B})$ for arbitrary polarization we use standard presentation of squared components of the polarization vector $e_\alpha e_\beta$ via the Stokes parameters, $P_{\rm L1} = \sin(4\phi)/2$, $P_{\rm L2} = [1+\cos(4\phi)]/2$, and $P_{\rm C} = \sin(2\phi)$, which are controlled by the orientation of the $\lambda/4$ plate, defined by the phase angle ϕ (see Suppl. Material). Simple calculation yields

$$U_{\rm A}^2 - U_{\rm B}^2 = E_0^2\left(a_0 + a_{\rm L1}P_{\rm L1} + a_{\rm L2}P_{\rm L2}\right)/2, \quad (5)$$
$$U_{\rm A}U_{\rm B}\sin(\varphi_{\rm A}-\varphi_{\rm B}) = E_0^2 a_{\rm C}P_{\rm C}/2, \quad (6)$$

where

$$a_0 = R_{\rm A}^2 - R_{\rm B}^2,\ \ a_{\rm L2} + i a_{\rm L1} = R_{\rm A}^2 e^{2i\theta_{\rm A}} - R_{\rm B}^2 e^{2i\theta_{\rm B}},$$
$$a_{\rm C} = -R_{\rm A}R_{\rm B}\sin(\theta_A - \theta_B),$$

are geometrical gate- and frequency- independent coefficients, which can be considered as fitting parameters for a more realistic model of antennas. The photoresponse reads

$$U(\phi) = \frac{F_1E_0^2}{2}\left[a_0 + a_{\rm L1}\frac{\sin(4\phi)}{2} + a_{\rm L2}\frac{1+\cos(4\phi)}{2}\right] + \frac{F_2E_0^2}{2}\,a_{\rm C}\sin(2\phi). \quad (7)$$

where[37,38]

$$F_{1,2} = \frac{\omega\ \alpha_{1,2}}{4U_{\rm g}\left|\sin(kL)\right|^2\sqrt{\omega^2+\gamma^2}} \quad (8)$$

are gate- and frequency-dependent factors, $k = \sqrt{\omega(\omega+\gamma)}/s$ is the plasma wave vector, $s \propto |U_g|^{1/4}$ is the plasma wave velosity, and L is the length of the gated region. The factor $\sin(kL)$ in denominator is responsible for plasmonic resonances, and the most general form of coefficients $\alpha_{1,2}$[37,38] is cumbersome and is presented in the Suppl. Material.

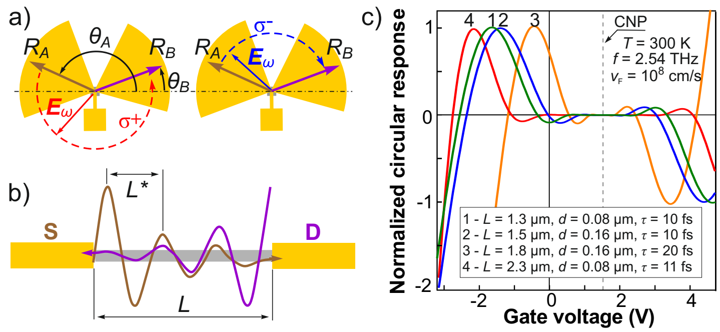

Figure 5: Panels (a) and (b) illustrate the physics behind the circular photoresponse caused by the plasmonic interference. (a) Bent bow-tie antenna characterized with two vectors $\mathbf{R}_{\mathrm{A}}$ and $\mathbf{R}_{\mathrm{B}}$, (see also Fig. 2 in the Suppl. Material) along with the hodograph of the electric filed in case of circularly polarized for positive (left, red arrow) and negative (right, blue arrow) helicities. Due to opposite rotation direction, the phase differences between the source and drain potentials have opposite signs for opposite helicities. (b) Illustration of plasma waves excited at the source and drain electrodes. (c) Calculated gate dependence of the interference part of the response for different parameters. The vertical dashed line corresponds to CNP.

Comparing Eq. (7) with empirical Eq. (1) we conclude that the data shown in the Fig. 2 are fully consistent with theory. The coefficients in the empirical formula can be written as follows: $U_{\mathrm{C}} = F_2 E_0^2 a_{\mathrm{C}}/2$, and $U_\alpha = F_1 E_0^2 a_\alpha/2$ for $\alpha = 0, \mathrm{L}_1, \mathrm{L}_2$. In particular, the interference-induced helicity-sensitive contribution, $\propto F_2$, is clearly observed in the experiment, see Fig. 2. This contribution can be easily extracted from the response

$$U_{\mathrm{C}} = -F_2 \frac{E_0^2 R_{\mathrm{A}} R_{\mathrm{B}}}{2} \sin(\theta_{\mathrm{A}} - \theta_{\mathrm{B}}). \qquad (9)$$

Physically, the interference contribution appears when source and drain electrodes "talk" to each other via exchange of plasma wave phase-shifted excitations. To clarify this point, we consider the non-resonant regime, $s/L \ll \gamma$, $\omega \ll \gamma$, which corresponds to our experimental situation. From the experimental conductance curves the scattering rate γ is estimated to be about 50 THz, which is much larger than the radiation frequency 2.54 THz used in our work. In this case, plasma waves decay from the source and drain part of the channel within the length $L_* = s\sqrt{2}/\sqrt{\omega\gamma}$, and the parameters $F_{1,2}$ in Eq. (7) are given by

$$F_1 = \frac{1}{4U_{\mathrm{g}}}, \quad F_2 = \frac{4\omega}{\gamma} \frac{\sin\left(L/L_*\right) e^{-L/L_*}}{U_{\mathrm{g}}}. \qquad (10)$$

Hence, the characteristic length of plasma wave decay L_* should not be too small as compared to L, so that plasmons excited near the source and drain electrodes could efficiently interfere within the channel, see the Fig. 5b. As the gate voltage controls the type and concentration of the charge carriers it also controls s and L_*. As a result, F_2 and, consequently, the helicity-sensitive part of the response oscillates as a function of the gate voltage. In our experiment L_* was essentially smaller than: $L_* \sim (0.1 \div 0.3)L$. However, the interference helicity-dependent part of the response was clearly seen in the experiment. The result of the calculations are presented in Fig. 5c. We obtain a qualitative agreement of the calculations and results of the experiments presented in Fig. 3a:

- the circular photoresponse at high positive gate voltages and for moderate negative U_{g} have an opposite sign;
- with an increase of the negative gate voltages value the response changes its sign;
- in the vicinity of the Dirac point, circular response oscillates.

The last statement needs clarification. While the oscillations are not visible in U_{C} (magenta curve of Fig. 3a), in individual curves obtained for left- (blue curve) and right- (red curve) polarizations they are clearly present. This difference is caused by the fact that the U_{σ^+} and U_{σ^-} curves represent the results of two different experiments, namely, measurements for σ^+ and σ^- radiation. At the same time, U_C is obtained as a result of subtraction of these two curves, corresponding to different U_g sweeps. Due to the hysteresis of the R_{xx} discussed above in Sec. 2, the sample parameters were slightly different for these two measurements and the oscillations present in one curve are superimposed with a larger featureless signal from the other. Fig. 3b shows the presence of the oscillations in photoresponse to circularly polarized radiation for the second device too.

Now we estimate the period of the oscillations. The dependence on the gate voltage is mostly encoded in $L_* \propto U_g{}^{1/4}$. The oscillations period can be estimated from the condition $\delta(L/L_*) \sim 1$, which gives $(L/L_*)\delta U_g/4U_g \sim 1$. For $U_g \approx 2$ V and $L_*/L \approx 0.1$, we find $\delta U_g \approx 0.8$ V in a good agreement with the experiment. We also note that the experimentally observed oscillations (see the blue curve for the device 1) decay at the same scale as an oscillation period in an excellent agreement with the behavior of the function F_2, see Eq. (10). Importantly, the key parameter $L_*/L = s\sqrt{2}/L\sqrt{\omega\gamma}$ depends on plasma velocity, mobility, and frequency. High mobility of graphene makes it one of the best candidates for THz interferometer as compared to Si, AlGaN/GaN, ALGaN/InGaAs, and p-diamond.[71]

We emphasize that the presence of oscillations is the hallmark of the interference part of the response. The response to the linearly polarized radiation does not show any oscillations in the vicinity of the CNP, see Fig. 4b. By contrast, it just follows to $(dG/dU_g)/G$ — a well-known behavior for Dyakonov-Shur noncoherent plasmonic detectors,[50] see expression for F_1 in Eq. (10).

Summary

To summarize, we demonstrated that specially designed graphene-based FET can be used to study plasma wave interference effects. Our approaches can be extrapolated to other 2D materials and used as a tool to characterize optically-induced plasmonic excitations. The conversion of the interfering plasma waves into dc response is controlled by the gate voltage and encodes information about helicity of the radiation and phase difference between the plasmonic signals. Our work shows that CVD graphene with moderate mobility, which is compatible with most standard technological routes can be used as a material for active plasmonic devices. We suggest a broad-band helicity-sensitive interferometer capable of analyzing both polarization of THz radiation and geometrical phase shift caused by antennas asymmetry. Such a device can be tuned to detect individual Stokes parameters. Hence, our work paves a novel way of developing the all-electric detectors of the terahertz radiation polarization state.

Acknowledgement The experimental part of this work was supported by the FLAG-ERA program (project DeMeGRaS, project GA501/16-1 of the DFG), the Russian Foundation for Basic Research within Grants No. 18-37-20058 and No. 18-29-20116, the Volkswagen Stiftung Program (97738). V.K. and I.G. acknowledge support of Russian Science Foundation (Grant No. 20-12-00147) and Foundation for the Advancement of Theoretical Physics and Mathematics BASIS in the development of theoretical interpretation. M.M. acknowledges support of Russian Science Foundation (project No. 17-72-30036) in sample design. The work in Poland was supported by Foundation for Polish Science (IRA Program, grant MAB/2018/9, CENTERA).

Notes. The authors declare no competing financial interest.

Supporting Information Available

Technical theoretical information and experimental methodology.

This material is available free of charge via the internet at http://pubs.acs.org.

References

(1) Scully, M. O.; Zubairy, M. S. *Quantum Optics*; Cambridge University Press: Cambridge, 1997.

(2) Hariharan, P. *Basics of Interferometry*; Academic Press: Amsterdam, 2007.

(3) Demkowicz-Dobrzański, R.; Jarzyna, M.; Kołodyński, J. *Progress in Optics*; Elsevier, 2015; pp 345–435.

(4) Pan, J.-W.; Chen, Z.-B.; Lu, C.-Y.; Weinfurter, H.; Zeilinger, A.; Żukowski, M. Multiphoton entanglement and interferometry. *Rev. Mod. Phys.* **2012**, *84*, 777–838.

(5) Ganichev, S.; Yemelyanov, S.; Ivchenko, E.; Perlin, E.; Terent'ev, Y.; Fedorov, A.; Yaroshetskii, I. Multiphoton absorption in semiconductors at submillimeter wavelengths. *J. Exp. Theor. Phys.* **1986**, *64*, 729–737.

(6) Keay, B. J.; Allen, S. J.; Galán, J.; Kaminski, J. P.; Campman, K. L.; Gossard, A. C.; Bhattacharya, U.; Rodwell, M. J. W. Photon-Assisted Electric Field Domains and Multiphoton-Assisted Tunneling in Semiconductor Superlattices. *Phys. Rev. Lett.* **1995**, *75*, 4098–4101.

(7) Boal, D. H.; Gelbke, C.-K.; Jennings, B. K. Intensity interferometry in subatomic physics. *Rev. Mod. Phys.* **1990**, *62*, 553–602.

(8) Cronin, A. D.; Schmiedmayer, J.; Pritchard, D. E. Optics and interferometry with atoms and molecules. *Rev. Mod. Phys.* **2009**, *81*, 1051–1129.

(9) Uzan, A. J.; Soifer, H.; Pedatzur, O.; Clergerie, A.; Larroque, S.; Bruner, B. D.; Pons, B.; Ivanov, M.; Smirnova, O.; Dudovich, N. Spatial molecular interferometry via multidimensional high-harmonic spectroscopy. *Nat. Photonics* **2020**, *14*, 188–194.

(10) Becker, D. et al. Space-borne Bose–Einstein condensation for precision interferometry. *Nature* **2018**, *562*, 391–395.

(11) Danner, A.; Demirel, B.; Kersten, W.; Lemmel, H.; Wagner, R.; Sponar, S.; Hasegawa, Y. Spin-rotation coupling observed in neutron interferometry. *Npj Quantum Inf.* **2020**, *6*, 23.

(12) Yin, B.; Piao, Z.; Nishimiya, K.; Hyun, C.; Gardecki, J. A.; Mauskapf, A.; Jaffer, F. A.; Tearney, G. J. 3D cellular-resolution imaging in arteries using few-mode interferometry. *Light: Sci. Appl.* **2019**, *8*, 104.

(13) Spahr, H.; Pfäffle, C.; Burhan, S.; Kutzner, L.; Hilge, F.; Hüttmann, G.; Hillmann, D. Phase-sensitive interferometry of decorrelated speckle patterns. *Sci. Rep.* **2019**, *9*, 11748.

(14) Shevchenko, S.; Ashhab, S.; Nori, F. Landau–Zener–Stückelberg interferometry. *Phys. Rep.* **2010**, *492*, 1–30.

(15) Wang, Z.; Huang, W.-C.; Liang, Q.-F.; Hu, X. Landau-Zener-Stückelberg Interferometry for Majorana Qubit. *Sci. Rep.* **2018**, *8*, 7920.

(16) Saha, S. K. Modern optical astronomy: technology and impact of interferometry. *Rev. Mod. Phys.* **2002**, *74*, 551–600.

(17) Goda, K.; Miyakawa, O.; Mikhailov, E. E.; Saraf, S.; Adhikari, R.; McKenzie, K.; Ward, R.; Vass, S.; Weinstein, A. J.; Mavalvala, N. A quantum-enhanced prototype gravitational-wave detector. *Nat. Phys.* **2008**, *4*, 472–476.

(18) Adhikari, R. X. Gravitational radiation detection with laser interferometry. *Rev. Mod. Phys.* **2014**, *86*, 121–151.

(19) Sala, S.; Ariga, A.; Ereditato, A.; Ferragut, R.; Giammarchi, M.; Leone, M.; Pistillo, C.; Scampoli, P. First demonstration of antimatter wave interferometry. *Sci. Adv.* **2019**, *5*, eaav7610.

(20) Gramotnev, D. K.; Bozhevolnyi, S. I. Plasmonics beyond the diffraction limit. *Nat. Photonics* **2010**, *4*, 83–91.

(21) Graydon, O. Plasmonic interferometry. *Nat. Photonics* **2012**, *6*, 139–139.

(22) Ali, J.; Pornsuwancharoen, N.; Youplao, P.; Aziz, M.; Chiangga, S.; Jaglan, J.; Amiri, I.; Yupapin, P. A novel plasmonic interferometry and the potential applications. *Results Phys.* **2018**, *8*, 438–441.

(23) Khajemiri, Z.; Hamidi, S.; Suwal, O. K. Highly sensitive biochemical sensor based on nanostructured plasmonic interferometer. *Opt. Commun.* **2018**, *427*, 85–89.

(24) Khajemiri, Z.; Lee, D.; Hamidi, S. M.; Kim, D.-S. Rectangular plasmonic interferometer for high sensitive glycerol sensor. *Sci. Rep.* **2019**, *9*, 1378.

(25) Zhang, Z.; Chen, Y.; Liu, H.; Bae, H.; Olson, D. A.; Gupta, A. K.; Yu, M. On-fiber plasmonic interferometer for multi-parameter sensing. *Opt. Express* **2015**, *23*, 10732–10740.

(26) Salamin, Y.; Benea-Chelmus, I.-C.; Fedoryshyn, Y.; Heni, W.; Elder, D. L.; Dalton, L. R.; Faist, J.; Leuthold, J. Compact and ultra-efficient broadband plasmonic terahertz field detector. *Nat. Commun.* **2019**, *10*, 5550.

(27) Yuan, G.; Rogers, E. T. F.; Zheludev, N. I. "Plasmonics" in free space: observation of giant wavevectors, vortices, and energy backflow in superoscillatory optical fields. *Light: Sci. Appl.* **2019**, *8*, 2.

(28) Woessner, A.; Gao, Y.; Torre, I.; Lundeberg, M. B.; Tan, C.; Watanabe, K.; Taniguchi, T.; Hillenbrand, R.; Hone, J.; Polini, M.; Koppens, F. H. L. Electrical 2π phase control of infrared light in a 350-nm footprint using graphene plasmons. *Nat. Photonics* **2017**, *11*, 421–424.

(29) Smolyaninov, A.; Amili, A. E.; Vallini, F.; Pappert, S.; Fainman, Y. Programmable plasmonic phase modulation of free-space wavefronts at gigahertz rates. *Nat. Photonics* **2019**, *13*, 431–435.

(30) Hakala, T. K.; Moilanen, A. J.; Väkeväinen, A. I.; Guo, R.; Martikainen, J.-P.; Daskalakis, K. S.; Rekola, H. T.; Julku, A.; Törmä, P. Bose–Einstein condensation in a plasmonic lattice. *Nat. Phys.* **2018**, *14*, 739–744.

(31) Dennis, B. S.; Haftel, M. I.; Czaplewski, D. A.; Lopez, D.; Blumberg, G.; Aksyuk, V. A. Compact nanomechanical plasmonic phase modulators. *Nat. Photonics* **2015**, *9*, 267–273.

(32) Haffner, C. et al. All-plasmonic Mach–Zehnder modulator enabling optical high-speed communication at the microscale. *Nat. Photonics* **2015**, *9*, 525–528.

(33) Mittleman, D. *Sensing with Terahertz Radiation*; Springer Series in Optical Sciences: Berlin, 2010.

(34) Dhillon, S. S. et al. The 2017 terahertz science and technology roadmap. *J. Phys. D: Appl. Phys.* **2017**, *50*, 043001.

(35) Drexler, C.; Dyakonova, N.; Olbrich, P.; Karch, J.; Schafberger, M.; Karpierz, K.; Mityagin, Y.; Lifshits, M. B.; Teppe, F.; Klimenko, O.; Meziani, Y. M.; Knap, W.; Ganichev, S. D. Helicity sensitive terahertz radiation detection by field effect transistors. *J. Appl. Phys.* **2012**, *111*, 124504.

(36) Romanov, K. S.; Dyakonov, M. I. Theory of helicity-sensitive terahertz radiation detection by field effect transistors. *Appl. Phys. Lett.* **2013**, *102*, 153502.

(37) Gorbenko, I. V.; Kachorovskii, V. Y.; Shur, M. S. Plasmonic Helicity-Driven Detector of Terahertz Radiation. *Phys. Status Solidi RRL* **2018**, 1800464.

(38) Gorbenko, I. V.; Kachorovskii, V. Y.; Shur, M. Terahertz plasmonic detector controlled by phase asymmetry. *Opt. Express* **2019**, *27*, 4004–4013.

(39) Dyakonov, M.; Shur, M. Shallow water analogy for a ballistic field effect transistor: New mechanism of plasma wave generation by dc current. *Phys. Rev. Lett.* **1993**, *71*, 2465–2468.

(40) Dyakonov, M.; Shur, M. Detection, mixing, and frequency multiplication of terahertz radiation by two-dimensional electronic fluid. *IEEE Trans. Electron Devices* **1996**, *43*, 380–387.

(41) Knap, W.; Dyakonov, M.; Coquillat, D.; Teppe, F.; Dyakonova, N.; Łusakowski, J.; Karpierz, K.; Sakowicz, M.; Valusis, G.; Seliuta, D.; Kasalynas, I.; Fatimy, A.; Meziani, Y. M.; Otsuji, T. Field Effect Transistors for Terahertz Detection: Physics and First Imaging Applications. *J. Infrared Millim. Terahertz Waves* **2009**, *30*, 1319–1337.

(42) Tauk, R.; Teppe, F.; Boubanga, S.; Coquillat, D.; Knap, W.; Meziani, Y. M.; Gallon, C.; Boeuf, F.; Skotnicki, T.; Fenouillet-Beranger, C.; Maude, D. K.; Rumyantsev, S.; Shur, M. S. Plasma wave detection of terahertz radiation by silicon field effects transistors: Responsivity and noise equivalent power. *Appl. Phys. Lett.* **2006**, *89*, 253511.

(43) Sakowicz, M.; Łusakowski, J.; Karpierz, K.; Grynberg, M.; Knap, W.; Köhler, K.; Valušis, G.; Gołaszewska, K.; Kamińska, E.; Piotrowska, A. Terahertz detection by two dimensional plasma field effect transistors in quantizing magnetic fields. *Appl. Phys. Lett.* **2008**, *92*, 203509.

(44) Knap, W.; Kachorovskii, V.; Deng, Y.; Rumyantsev, S.; Lü, J.-Q.; Gaska, R.; Shur, M. S.; Simin, G.; Hu, X.; Khan, M. A.; Saylor, C. A.; Brunel, L. C. Nonresonant detection of terahertz radiation in field effect transistors. *J. Appl. Phys.* **2002**, *91*, 9346–9353.

(45) Knap, W.; Deng, Y.; Rumyantsev, S.; Shur, M. S. Resonant detection of subterahertz and terahertz radiation by plasma waves in submicron field-effect transistors. *Appl. Phys. Lett.* **2002**, *81*, 4637–4639.

(46) Peralta, X. G.; Allen, S. J.; Wanke, M. C.; Harff, N. E.; Simmons, J. A.; Lilly, M. P.; Reno, J. L.; Burke, P. J.; Eisenstein, J. P. Terahertz photoconductivity and plasmon modes in double-quantum-well field-effect transistors. *Appl. Phys. Lett.* **2002**, *81*, 1627–1629.

(47) Otsuji, T.; Hanabe, M.; Ogawara, O. Terahertz plasma wave resonance of two-dimensional electrons in InGaP/InGaAs/GaAs high-electron-mobility transistors. **2004**, *85*, 2119–2121.

(48) Teppe, F.; Knap, W.; Veksler, D.; Shur, M. S.; Dmitriev, A. P.; Kachorovskii, V. Y.; Rumyantsev, S. Room-temperature plasma waves resonant detection of sub-terahertz radiation by nanometer field-effect transistor. *Appl. Phys. Lett.* **2005**, *87*, 052107.

(49) Teppe, F.; Veksler, D.; Kachorovski, V. Y.; Dmitriev, A. P.; Xie, X.; Zhang, X.-C.; Rumyantsev, S.; Knap, W.; Shur, M. S. Plasma wave resonant detection of femtosecond pulsed terahertz radiation by a nanometer field-effect transistor. *Appl. Phys. Lett.* **2005**, *87*, 022102.

(50) Veksler, D.; Teppe, F.; Dmitriev, A. P.; Kachorovskii, V. Y.; Knap, W.; Shur, M. S. Detection of terahertz radiation in gated two-dimensional structures governed by dc current. *Phys. Rev. B* **2006**, *73*, 125328.

(51) Derkacs, D.; Lim, S. H.; Matheu, P.; Mar, W.; Yu, E. T. Improved performance

of amorphous silicon solar cells via scattering from surface plasmon polaritons in nearby metallic nanoparticles. *Appl. Phys. Lett.* **2006**, *89*, 093103.

(52) Fatimy, A. E. et al. Terahertz detection by GaN/AlGaN transistors. *Electron. Lett* **2006**, *42*, 1342–1344.

(53) Vicarelli, L.; Vitiello, M. S.; Coquillat, D.; Lombardo, A.; Ferrari, A. C.; Knap, W.; Polini, M.; Pellegrini, V.; Tredicucci, A. Graphene field-effect transistors as room-temperature terahertz detectors. *Nat. Mater.* **2012**, *11*, 865–871.

(54) Koppens, F. H. L.; Mueller, T.; Avouris, P.; Ferrari, A. C.; Vitiello, M. S.; Polini, M. Photodetectors based on graphene, other two-dimensional materials and hybrid systems. *Nat. Nanotechnol.* **2014**, *9*, 780–793.

(55) Bandurin, D. A. et al. Resonant terahertz detection using graphene plasmons. *Nat. Commun.* **2018**, *9*, 5392.

(56) Yadav, D.; Tamamushi, G.; Watanabe, T.; Mitsushio, J.; Tobah, Y.; Sugawara, K.; Dubinov, A. A.; Satou, A.; Ryzhii, M.; Ryzhii, V.; Otsuji, T. Terahertz light-emitting graphene-channel transistor toward single-mode lasing. *Nanophotonics* **2018**, *7*, 741–752.

(57) Rybin, M.; Pereyaslavtsev, A.; Vasilieva, T.; Myasnikov, V.; Sokolov, I.; Pavlova, A.; Obraztsova, E.; Khomich, A.; Ralchenko, V.; Obraztsova, E. Efficient nitrogen doping of graphene by plasma treatment. *Carbon* **2016**, *96*, 196–202.

(58) Gayduchenko, I. A.; Fedorov, G. E.; Moskotin, M. V.; Yagodkin, D. I.; Seliverstov, S. V.; Goltsman, G. N.; Kuntsevich, A. Y.; Rybin, M. G.; Obraztsova, E. D.; Leiman, V. G.; Shur, M. S.; Otsuji, T.; Ryzhii, V. I. Manifestation of plasmonic response in the detection of sub-terahertz radiation by graphene-based devices. *Nanotechnology* **2018**, *29*, 245204.

(59) Ganichev, S. D.; Tarasenko, S. A.; Bel'kov, V. V.; Olbrich, P.; Eder, W.; Yakovlev, D. R.; Kolkovsky, V.; Zaleszczyk, W.; Karczewski, G.; Wojtowicz, T.; Weiss, D. Spin Currents in Diluted Magnetic Semiconductors. *Phys. Rev. Lett.* **2009**, *102*, 156602.

(60) Kvon, Z.-D.; Danilov, S. N.; Mikhailov, N. N.; Dvoretsky, S. A.; Prettl, W.; Ganichev, S. D. Cyclotron resonance photoconductivity of a two-dimensional electron gas in HgTe quantum wells. *Physica E Low Dimens. Syst. Nanostruct.* **2008**, *40*, 1885–1887.

(61) Bel'kov, V. V.; Ganichev, S. D.; Ivchenko, E. L.; Tarasenko, S. A.; Weber, W.; Giglberger, S.; Olteanu, M.; Tranitz, H.-P.; Danilov, S. N.; Schneider, P.; Wegscheider, W.; Weiss, D.; Prettl, W. Magneto-gyrotropic photogalvanic effects in semiconductor quantum wells. *J. Phys.: Condens. Matter* **2005**, *17*, 3405–3428.

(62) Bahaa E. A. Saleh, M. T. *Fundamentals of Photonics, 2 Volume Set (Wiley Series in Pure and Applied Optics)*; Wiley: New York, 2019.

(63) Weber, W.; Golub, L. E.; Danilov, S. N.; Karch, J.; Reitmaier, C.; Wittmann, B.; Bel'kov, V. V.; Ivchenko, E. L.; Kvon, Z. D.; Vinh, N. Q.; van der Meer, A. F. G.; Murdin, B.; Ganichev, S. D. Quantum ratchet effects induced by terahertz radiation in GaN-based two-dimensional structures. *Phys. Rev. B* **2008**, *77*, 245304.

(64) Fedorov, G.; Kardakova, A.; Gayduchenko, I.; Charayev, I.; Voronov, B. M.; Finkel, M.; Klapwijk, T. M.; Morozov, S.; Presniakov, M.; Bobrinetskiy, I.; Ibragimov, R.; Goltsman, G. Photothermoelectric response in asymmetric carbon nanotube devices exposed to sub-terahertz radiation. *Appl. Phys. Lett.* **2013**, *103*, 181121.

(65) Gabor, N. M.; Song, J. C. W.; Ma, Q.; Nair, N. L.; Taychatanapat, T.; Watanabe, K.; Taniguchi, T.; Levitov, L. S.; Jarillo-Herrero, P. Hot Carrier-Assisted Intrinsic Photoresponse in Graphene. *Science* **2011**, *334*, 648–652.

(66) Cai, X.; Sushkov, A. B.; Suess, R. J.; Jadidi, M. M.; Jenkins, G. S.; Nyakiti, L. O.; Myers-Ward, R. L.; Li, S.; Yan, J.; Gaskill, D. K.; Murphy, T. E.; Drew, H. D.; Fuhrer, M. S. Sensitive room-temperature terahertz detection via the photothermoelectric effect in graphene. *Nat. Nanotechnol.* **2014**, *9*, 814–819.

(67) Castilla, S.; Terrés, B.; Autore, M.; Viti, L.; Li, J.; Nikitin, A. Y.; Vangelidis, I.; Watanabe, K.; Taniguchi, T.; Lidorikis, E.; Vitiello, M. S.; Hillenbrand, R.; Tielrooij, K.-J.; Koppens, F. H. Fast and Sensitive Terahertz Detection Using an Antenna-Integrated Graphene pn Junction. *Nano Lett.* **2019**, *19*, 2765–2773.

(68) Karch, J. et al. Dynamic Hall Effect Driven by Circularly Polarized Light in a Graphene Layer. *Phys. Rev. Lett.* **2010**, *105*, 227402.

(69) Jiang, C.; Shalygin, V. A.; Panevin, V. Y.; Danilov, S. N.; Glazov, M. M.; Yakimova, R.; Lara-Avila, S.; Kubatkin, S.; Ganichev, S. D. Helicity-dependent photocurrents in graphene layers excited by midinfrared radiation of a CO_2laser. *Phys. Rev. B* **2011**, *84*, 125429.

(70) Glazov, M.; Ganichev, S. High frequency electric field induced nonlinear effects in graphene. *Phys. Rep.* **2014**, *535*, 101–138.

(71) Liu, X.; Ytterdal, T.; Shur, M. Plasmonic FET Terahertz Spectrometer. *IEEE Access* **2020**, *8*, 56039–56044.

Graphical TOC Entry